Eur. Phys. J. D (2020) 74: 36
https://doi.org/10.1140/epjd/e2020-100549-0

THE EUROPEAN PHYSICAL JOURNAL D

Topical Review

Electron-scattering on molecular hydrogen: convergent close-coupling approach*

Liam H. Scarlett[1,a], Jeremy S. Savage[1], Dmitry V. Fursa[1], Igor Bray[1], and Mark C. Zammit[2]

[1] Curtin Institute for Computation and Department of Physics and Astronomy, Curtin University, Perth, Western Australia 6102, Australia
[2] Theoretical Division, Los Alamos National Laboratory, Los Alamos, NM 87545, USA

Received 31 October 2019 / Received in final form 26 December 2019
Published online 20 February 2020
© EDP Sciences / Società Italiana di Fisica / Springer-Verlag GmbH Germany, part of Springer Nature, 2020

Abstract. Calculations of electron-impact excitation cross sections for molecular hydrogen have been performed using spherical- and spheroidal-coordinate formulations of the molecular convergent close-coupling method. We present a comparison and find good agreement between the results of these two techniques performed within the fixed-nuclei approximation for excitation from the ground $X\ ^1\Sigma_g^+(v=0)$ state of H_2 to the $B\ ^1\Sigma_u^+$, $C\ ^1\Pi_u$, $B'\ ^1\Sigma_u^+$, $D\ ^1\Pi_u$, $E,F\ ^1\Sigma_g^+$, $b\ ^3\Sigma_u^+$, $c\ ^3\Pi_u$, $a\ ^3\Sigma_g^+$, $e\ ^3\Sigma_u^+$, $h\ ^3\Sigma_g^+$, and $d\ ^3\Pi_u$ states. For the spheroidal-coordinate approach the adiabatic-nuclei method has been applied, allowing for a more reliable estimate of cross sections at near-threshold energies. Comparison of the adiabatic-nuclei cross sections with the corresponding fixed-nuclei cross sections is also presented.

1 Introduction

Molecular hydrogen is the simplest neutral molecule. It is the most abundant molecule in the universe and is an important constituent of plasmas with applications in astrophysics, fusion, atmospheric physics, and various industries [1–7]. Elemental collision processes play an important role in modelling these plasmas, and collisions with electrons have attracted significant interest from both experiment and theory. A number of compilations of cross sections for electron collisions with molecular hydrogen have been produced [8–13], and a recommended set of cross sections was suggested by Yoon et al. [14].

In all cases these cross section data sets have been produced from an analysis of experimental data, even though there were significant discrepancies between different experiments for many transitions. Theoretical calculations have been largely excluded from critical evaluations of the data due to large uncertainties. This changed with the application of the convergent close-coupling (CCC) method to electron collisions with molecules [15–17]. A comprehensive data set of cross sections for elastic scattering, excitation of a large number of singlet and triplet states, ionisation, stopping power, and total cross sections for e^--H_2 scattering have been produced. The distinctive feature of the molecular CCC (MCCC) calculations was an explicit demonstration of convergence in the cross sections achieved by performing calculations with the size of the close-coupling expansion ranging from 9 to 491 target states.

The MCCC calculations were performed in a single-centre spherical-coordinate formulation using the fixed-nuclei (FN) approximation, with target wave functions being of similar or somewhat better quality than those used in previous calculations [18–30], for example in the R-matrix (RM) [28,29] and the Schwinger multichannel (SMC) [30] calculations. We do not expect the approximations in the MCCC method to lead to significant errors except at near-threshold energies where the FN approximation fails. The large discrepancies identified with previous results, even for the strong transitions of fundamental importance such as excitation of the dissociative $b\ ^3\Sigma_u^+$ state, were a matter of concern. It was therefore significant that the recent measurements of e^--H_2 excitation cross sections [31,32] conducted at California State University proved to be in much better agreement with the MCCC calculations; for the $b\ ^3\Sigma_u^+$ state the agreement was nearly perfect [33,34].

To further verify the accuracy of the MCCC calculations we have developed a formulation of the MCCC method in the prolate spheroidal coordinate system. Spheroidal coordinates are the natural choice for describing diatomic molecules as they allow for a more accurate account of the lack of spherical symmetry and multi-centre nature of the scattering system. In the context of electron collisions

* Contribution to the Topical Issue "Low-Energy Positron and Positronium Physics and Electron-Molecule Collisions and Swarms (POSMOL 2019)" edited by Michael Brunger, David Cassidy, Saša Dujko, Dragana Marić, Joan Marler, James Sullivan, Juraj Fedo.

[a] e-mail: liam.scarlett@postgrad.curtin.edu.au

this approach allows us to perform calculations at larger internuclear separations than possible with the spherical-coordinate implementation, thereby enabling the application of the adiabatic-nuclei (AN) method [35] and generation of cross sections for transitions between vibrational levels in the initial and final electronic states. Such cross sections are important in many applications, as molecular hydrogen is present in astrophysical, fusion, and technological plasmas in a range of vibrationally excited states. Determination of plasma properties and interpretation of the spectroscopic data relies on the availability of reliable collision data, including fully vibrationally resolved cross sections [36–38]. The capacity to produce such data sets has allowed us to perform a detailed study of dissociation processes involving molecular hydrogen in the ground and vibrationally excited states [39–42], and study vibrational excitation of the $X\ ^1\Sigma_g^+$ ground state via electron-impact excitation and radiative cascade [43].

The main purpose of this paper is to present a systematic comparison of the cross sections obtained in the spherical and spheroidal formulations of the MCCC method. In the next section a brief outline of the theoretical methods is presented. In Section 3 the details of the calculations are presented and in Section 4 we present a comparison of the results from the spherical and spheroidal formulations of the MCCC method for excitation of the $B\ ^1\Sigma_u^+$, $C\ ^1\Pi_u$, $B'\ ^1\Sigma_u^+$, $D\ ^1\Pi_u$, $E, F\ ^1\Sigma_g^+$, $b\ ^3\Sigma_u^+$, $c\ ^3\Pi_u$, $a\ ^3\Sigma_g^+$, $e\ ^3\Sigma_u^+$, $h\ ^3\Sigma_g^+$, and $d\ ^3\Pi_u$ states from the ground $X\ ^1\Sigma_g^+(v=0)$ state. Conclusions and future directions are discussed in Section 5. Atomic units are used throughout the paper except where specified otherwise.

2 Theory

The details for the application of the MCCC method to electron-molecule scattering have been presented in a number of publications [16,17,44,45]. Here we give a brief overview with the emphasis being on the differences between the spherical- and spheroidal-coordinate implementations.

We start with the FN formulation, where the nuclei are kept at a fixed orientation and internuclear separation R. The Born-Oppenheimer approximation allows the nuclear and electronic degrees of freedom to be separated, reducing the scattering problem to solving for the electronic scattering wave function with R treated as a fixed parameter. The scattering equations are formulated in the body frame, with the z axis aligned with the internuclear axis. For the spherical formulation the origin is placed at the geometric centre of the two nuclei. For the spheroidal formulation the two focal points are chosen to coincide with the positions of the nuclei. With this choice the prolate spheroidal coordinates $\boldsymbol{\rho} = (\rho, \eta, \phi)$ are defined as

$$\underset{0 \le \rho < \infty}{\rho = \frac{r_1 + r_2}{2} - \frac{R}{2}}, \quad \text{and} \quad \underset{-1 \le \eta \le 1}{\eta = \frac{r_1 - r_2}{R}}, \tag{1}$$

where r_1 and r_2 are the distances from the two focal points. Note that we have modified the radial variable from the standard definition ($\xi = (r_1 + r_2)/R$) to avoid the singularity at the combined-nuclear limit ($R = 0$). In this limit it is easy to show that the spheroidal coordinates we have adopted (1) reduce to the standard spherical coordinates $\boldsymbol{r} = (r, \theta, \phi)$:

$$\lim_{R\to 0} \rho = r, \qquad \lim_{R\to 0} \eta = \cos\theta. \tag{2}$$

The azimuthal angle ϕ retains the same definition in both coordinate systems.

In the close-coupling approach to electron-molecule collisions the total wave function of the collision system is expanded in the set of the N target states:

$$\begin{aligned}\Psi_i^{N(+)}(\bar{\boldsymbol{x}}_0, \bar{\boldsymbol{x}}_1, \bar{\boldsymbol{x}}_2) &= \mathcal{A}\psi_i^{N(+)}(\bar{\boldsymbol{x}}_0, \bar{\boldsymbol{x}}_1, \bar{\boldsymbol{x}}_2) \\ &= \mathcal{A}\sum_{n=1}^{N} f_n^{N(+)}(\bar{\boldsymbol{x}}_0)\Phi_n^N(\bar{\boldsymbol{x}}_1, \bar{\boldsymbol{x}}_2),\end{aligned} \tag{3}$$

where $\bar{\boldsymbol{x}} = \{\boldsymbol{x}, \sigma\}$ is used to denote both the spatial $\boldsymbol{x}$ and spin σ coordinates and $\boldsymbol{x}$ stands for the spherical ($\boldsymbol{r}$) or spheroidal ($\boldsymbol{\rho}$) representations. The projectile coordinates are assigned the index 0, while the indices 1 and 2 refer to the target electrons. The (+) superscript denotes outgoing spherical boundary conditions, and $\mathcal{A}$ is the antisymmetrisation operator. The explicit dependence on R has been suppressed for clarity of presentation and will be restored when required.

The electronic target states of H_2 are characterised by conserved quantum numbers of orbital angular momentum projection m_n, parity π_n, and spin s_n, and are constructed from antisymmetrised two-electron functions:

$$\Phi_n^N(\bar{\boldsymbol{x}}_1, \bar{\boldsymbol{x}}_2) = \sum_{\alpha\beta} C_{\alpha\beta}^{(n)} \phi_\alpha(\boldsymbol{x}_1)\phi_\beta(\boldsymbol{x}_2) X_{m_{s_n}}^{s_n}(\sigma_1, \sigma_2), \tag{4}$$

where $X_{m_{s_n}}^{s_n}(\sigma_1, \sigma_2)$ is the two-electron spin function and the configuration-interaction (CI) coefficients are denoted by $C_{\alpha\beta}^{(n)}$. The CI coefficients satisfy $C_{\alpha\beta}^{(n)} = (-1)^{s_n} C_{\beta\alpha}^{(n)}$ to ensure the antisymmetry of the target states, and are obtained via diagonalisation of the target Hamiltonian for each target symmetry (m, π, s). The target states satisfy

$$\langle \Phi_{n'}^N | H_{\mathrm{T}} | \Phi_n^N \rangle = \epsilon_n^N \delta_{n'n}, \tag{5}$$

where ϵ_n^N is the electronic energy of the state Φ_n^N.

The one-electron functions in equation (4) are characterised by orbital angular momentum ℓ_α, parity $\pi_\alpha = (-1)^{\ell_\alpha}$, and orbital angular momentum projection m_α, and are expressed as

$$\phi_\alpha(\boldsymbol{x}) = \varphi_{k_\alpha\{\ell_\alpha, m_\alpha\}}(x) Y_{\ell_\alpha m_\alpha}(\hat{\boldsymbol{x}}), \tag{6}$$

where $Y_{\ell m}(\hat{\boldsymbol{x}})$ is a spherical harmonic. The radial components are the Laguerre basis functions given for the spherical formulation by

$$\varphi_{k\ell}(r) = \sqrt{\frac{\alpha_\ell (k-1)!}{(k+\ell)(k+2\ell)!}} (2\alpha_\ell r)^\ell e^{-\alpha_\ell r} L_{k-1}^{2\ell+1}(2\alpha_\ell r), \tag{7}$$

and for the spheroidal formation by

$$\varphi_{km}(\rho) = \sqrt{\frac{2\alpha_m(k-1)!}{(k+m-1)!}}(2\alpha_m\rho)^{m/2}e^{-\alpha_m\rho}L_{k-1}^{m}(2\alpha_m\rho). \tag{8}$$

Here, L_k^a are the associated Laguerre polynomials, and α is an exponential fall-off parameter.

The total wave function of the collision system satisfies the Schrödinger equation

$$(E^{(+)} - H)\Psi_i^{N(+)} = 0, \tag{9}$$

where $H = K_0 + V + H_T$ is the total (electronic) Hamiltonian, K_0 is the projectile kinetic-energy operator, and V is the projectile-target interaction potential. The MCCC method solves the Schrödinger equation by substitution of the expansion (3) for $\Psi_i^{N(+)}$, and formulating the set of close-coupling equations in momentum space for the T matrix

$$\langle \boldsymbol{k}_f^{(-)}\Phi_f^N|T^N|\Phi_i^N\boldsymbol{k}_i^{(+)}\rangle = \langle \boldsymbol{k}_f^{(-)}\Phi_f^N|V|\psi_i^{N(+)}\rangle. \tag{10}$$

The projectile distorted waves are the solutions of

$$(\epsilon_k - K_0 - U_0)|\boldsymbol{k}^{(\pm)}\rangle = 0, \tag{11}$$

where $\epsilon_k = k^2/2$ and U_0 is a short-ranged central distorting potential taken as the spherically symmetric part of the electron-molecule direct potential averaged over the ground (electronic) state of H_2. The close-coupling equations are solved by performing a partial-wave expansion of the distorted waves, which for the spherical formulation is given by

$$|\boldsymbol{k}^{(\pm)}\rangle = \frac{1}{k}\sum_{L,M} i^L e^{\pm i\delta_L}Y_{LM}^*(\hat{\boldsymbol{k}})|kL\rangle, \tag{12}$$

where δ_L is the distorting phase shift and the sum is taken to some maximum value $L_{\max}$ and $|M| \le L_{\max}$. For the spheroidal formulation the spherical harmonics in equation (12) are replaced by the spheroidal harmonics, and the radial and angular equations are solved as discussed in reference [46].

The resulting Lippmann-Schwinger equations for the partial-wave T matrix are given by

$$T^{M\Pi S}_{fL_fM_f,iL_iM_i}(k_f,k_i) = V^{M\Pi S}_{fL_fM_f,iL_iM_i}(k_f,k_i) + \sum_{n=1}^{N}\sum_{LM}\sum\!\!\!\!\!\!\int_k \mathrm{d}k \frac{V^{M\Pi S}_{fL_fM_f,nLM}(k_f,k)\,T^{M\Pi S}_{nLM,iL_iM_i}(k,k_i)}{E-\epsilon_k-\epsilon_n^N+i0}. \tag{13}$$

These equations are solved for each partial wave of the total orbital angular momentum projection M, parity Π, and spin S using standard techniques [47]. The body-frame T matrix is transformed to the laboratory frame and an orientation-averaging procedure is performed to produce cross sections of interest [44]. For example, the FN partial-wave integrated cross sections (ICS) are calculated from the partial-wave T-matrix elements in the following way:

$$\sigma_{f,i}^{M\Pi S} = \frac{q_f}{q_i}\frac{1}{4\pi}\sum_{\substack{L_f,L_i\\M_f,M_i}}\left|F^{M\Pi S}_{fL_fM_f,iL_iM_i}\right|^2, \tag{14}$$

where

$$F^{M\Pi S}_{fL_fM_f,iL_iM_i} = -(2\pi)^2(q_fq_i)^{-1}i^{L_i-L_f} \times T^{M\Pi S}_{fL_fM_f,iL_iM_i}(q_f,q_i), \tag{15}$$

and q is the linear momentum of the projectile which is used to indicate the physical T-matrix elements. The spin-averaged ICS is given by

$$\sigma_{f,i} = \sum_S \frac{2S+1}{2(2s_i+1)}\sum_{M\Pi}\sigma_{f,i}^{M\Pi S}, \tag{16}$$

where s_i is the initial target-state spin. For scattering on the ground state of H_2, $s_i = 0$ and hence there is only one spin channel.

The partial-wave expansion (16) of the cross sections converges slowly for dipole-allowed transitions at intermediate and large incident electron energies. To accelerate the convergence, the analytic Born subtraction (ABS) technique can be utilised. See details in reference [44] for applications of the ABS technique to both integrated and differential cross sections.

2.1 Adiabatic-nuclei approximation

The AN approximation provides a method for obtaining fully vibrationally resolved cross sections from the FN T matrix calculated over a range of internuclear separations R. The AN cross section for the transition $iv_i \to fv_f$ is given by

$$\sigma_{fv_f,iv_i} = \frac{q_{fv_f}}{4\pi q_i}\sum_{\substack{L_f,L_i\\M_f,M_i}}\left|\langle\nu_{fv_f}|F_{fL_fM_f,iL_iM_i}|\nu_{iv_i}\rangle_R\right|^2. \tag{17}$$

Here q_{fv_f} and q_i are the outgoing and incident projectile linear momenta, and ν_{nv_n} are the vibrational wave functions which are obtained by diagonalising the Born-Oppenheimer vibrational Hamiltonian

$$\mathcal{H}_n^{\mathrm{BO}} = -\frac{1}{2\mu}\frac{\mathrm{d}^2}{\mathrm{d}R^2} + \frac{J(J+1)-m_n^2}{2\mu R^2} + \epsilon_n(R) \tag{18}$$

in a basis of nuclear functions which have the same form as the one-electron functions (7). Here, μ is the nuclear reduced mass, ϵ_n is the potential-energy curve (PEC) of the electronic state n, J is the total molecular angular momentum, and m_n is the electronic-state angular momentum projection onto the internuclear axis. The centrifugal term in equation (18) can be neglected for small J, as it is insignificant compared to ϵ_n. The outgoing momentum q_{fv_f} satisfies the energy conservation relation

$$q_{fv_f} = \sqrt{2\left[E_{\mathrm{in}} - \varepsilon_{fv_f,iv_i}\right]}, \tag{19}$$

where ε_{fv_f,iv_i} is the vibrationally resolved excitation energy.

The integration over R in equation (17) requires the FN calculations to be performed on a sufficiently fine R mesh over the region where the initial vibrational wave function is non-negligible. This can lead to very substantial computational requirements when the calculations utilise large close-coupling expansions.

To compare the FN and AN cross sections we sum the vibrationally resolved cross sections (17) over the final vibrational levels, giving

$$\sigma_{f,iv_i} = \sum_{v_f} \sigma_{fv_f,iv_i}. \tag{20}$$

In the limit of neglecting the energy difference between the final vibrational levels, equation (20) takes the simple form

$$\sigma_{f,iv_i} \approx \langle \nu_{iv_i} | \sigma_{f,i} | \nu_{iv_i} \rangle_R \tag{21}$$

due to the completeness of the set of vibrational states $\{\nu_{fv_f}\}$. Here, $\sigma_{f,i}$ is the R-dependent FN cross section (16). If the R dependence of the FN cross section can be neglected over the region where the initial vibrational wave function is non-negligible then equation (21) reduces to the FN cross section (16). The last requirement can be relaxed by assuming a linear dependence of the FN cross section on R. Then performing the FN calculations at the average internuclear distance ($R_{\rm m} = 1.448$ for H_2) gives the best approximation to the corresponding AN cross section [48]. Note, however, that the FN method cannot reproduce the AN cross sections at near-threshold energies, where the R dependence of the cross sections must be taken into account.

3 Details of the calculations

The accuracy of the calculated collision data significantly depends on the accuracy of the underlying structure model. In this section we present an overview of the H_2 target structure adopted in the MCCC calculations performed in the spherical and spheroidal formulations. In general, the main aspects in adopting a target structure model for the H_2 molecule are:

(a) accounting for the multicentre and non-spherical nature of the problem,
(b) accounting for electron-electron correlations,
(c) implementing the above in a way that allows for tractable scattering calculations.

The spheroidal formulation is significantly more accurate in dealing with the multicentre and non-spherical issues. For both formulations we have used a two-step approach to building the target wave functions. First, a large Laguerre basis ($N_\ell = 60 - \ell, \ell \leq 8$) is used to obtain an accurate $1s\sigma_g$ orbital of the H_2^+ ion as it is most affected by the multicentre and non-spherical aspects. This step is performed with the internuclear separation of the ion equal to the separation R of the H_2 molecule. The second step is a standard two-electron configuration-interaction approach that makes use of a much smaller Laguerre basis together with the calculated $1s\sigma_g$ orbital in place of the $1s$ Laguerre function. The target model adopted in the spherical formulation has been described in reference [44]. The model has an underlying Laguerre basis with $N_\ell = 17 - \ell, \ell \leq 3$ and exponential falloffs $\alpha_0 = 0.76$, $\alpha_1 = 0.765$, $\alpha_2 = 0.79$, and $\alpha_3 = 0.85$, which provide a sufficiently accurate representation of the target states up to the $n = 4$ shell at $R = 1.448$. The CI expansion includes frozen-core configurations $(1s, nlm)$, and all $(nlm, n'l'm')$ correlation configurations with principle quantum numbers $n, n' \leq 2$. The maximum number of states generated in this model is 491, including 92 negative energy states (relative to the H_2^+ ground state), with the remaining states representing the ionisation continuum. The partial-wave expansion of the projectile continuum waves was performed up to $L_{\rm max} = 8$, and the maximum total angular momentum projection in the partial-wave expansion of the Lippmann-Schwinger equation (13) was chosen to be $M_{\rm max} = L_{\rm max}$. The MCCC(491) calculations require substantial computational resources and were performed at relatively few energies where experiment is available and which were sufficient to map all excitation cross sections. As the accuracy of the spherical formulation becomes poor at large internuclear separations, the scattering calculations were performed at $R = 1.448$ only, with the principle aim being to establish convergence in the calculated cross sections as discussed in reference [44]. This restriction on R limits the results to cross sections which are summed over final vibrational levels, for scattering on the $v_i = 0$ vibrational state only. In order to model scattering on excited vibrational levels and to obtain results for excitation of specific final vibrational levels the AN approximation must be utilised, which requires FN calculations to be performed over a range of R values.

The spheroidal calculations were performed with the aim of obtaining AN cross sections for excitation of a number of low-lying electronic states. This requires a large number of calculations to be performed at many internuclear distances R for each incident electron energy and makes it impractical to use a model as large as the MCCC(491) model discussed above. We have adopted a model with an underlying Laguerre basis of $N_\ell = 12 - \ell, \ell \leq 3$ functions and exponential falloffs $\alpha = 0.8$ for each m. The CI expansion includes all frozen-core configurations $(1s, nlm)$, as well as correlation configurations $(n\ell m, n'\ell'm')$ with $n\ell, n'\ell'$ spanning the $1s$, $2s$, $3s$, $2p$, $3p$, $3d$, $4d$, $5d$, and $4f$ orbitals. To account for the molecule becoming more diffuse at larger internuclear separations, these core orbitals were taken from a Laguerre basis with modified exponential falloffs which were optimised as a function of R to yield more accurate target states. At $R = 1.448$ the core orbitals have $\alpha_0 = 1.2$ and $\alpha_{m\geq 1} = 1.627$. At larger R the exponential falloffs are reduced to produce more diffuse orbitals, for example at $R = 5.0$ we used $\alpha_0 = 0.975$ and $\alpha_{m\geq 1} = 1.3$. The large number of correlation configurations in the spheroidal calculations was necessary to achieve sufficiently accurate target wave functions across all internuclear distances up to $R \approx 8.0$. The total number of states included in the scattering calculations is 210, including 56 discrete

Table 1. Two-electron energies of electronic target states of H_2 at the internuclear distance $R_0 = 1.4\ a_0$. Comparison of the present spherical- and spheroidal-coordinate calculations is made with accurate structure calculations [50–58].

State	Spherical	Spheroidal	Ref.
$X\ ^1\Sigma_g^+$	−1.162	−1.170	−1.174 [51]
$b\ ^3\Sigma_u^+$	−0.770	−0.784	−0.784 [52]
$a\ ^3\Sigma_g^+$	−0.710	−0.713	−0.714 [53]
$c\ ^3\Pi_u$	−0.701	−0.706	−0.707 [54]
$B\ ^1\Sigma_u^+$	−0.697	−0.705	−0.706 [55]
$E, F\ ^1\Sigma_g^+$	−0.687	−0.691	−0.692 [56]
$C\ ^1\Pi_u$	−0.683	−0.688	−0.689 [50]
$e\ ^3\Sigma_u^+$	−0.640	−0.643	−0.644 [57]
$h\ ^3\Sigma_g^+$	−0.628	−0.630	−0.630 [58]
$d\ ^3\Pi_u$	−0.626	−0.629	−0.629 [59]
$B'\ ^1\Sigma_u^+$	−0.625	−0.628	−0.629 [55]
$D\ ^1\Pi_u$	−0.621	−0.623	−0.624 [50]

states at $R = 1.448$. The projectile partial-wave expansion includes angular momenta up to $L_{max} = 6$ for incident electron energies below 20 eV and $L_{max} = 10$ at larger energies. At $R = 1.448$ the MCCC(210) calculations were performed on a fine energy mesh with the aim of resolving resonance behaviour and comparing with AN calculations.

To limit the computational resources we have developed a scaling procedure which makes use of collision data obtained with a significantly smaller close-coupling expansion. The MCC(27) model includes only the first 27 bound states from the MCCC(210) model. Scattering calculations have been performed with the MCC(27) model on a fine grid of internuclear separations. The scaling procedure is discussed in detail in reference [40]. We use the same MCCC(210) label to indicate AN collision data obtained with this procedure.

In Table 1 we present the two-electron energies for a number of low-lying states calculated at the internuclear distance $R = 1.4$ in both the spherical and spheroidal techniques, and compare with accurate structure calculations [50–59]. The spheroidal approach clearly demonstrates a high level of accuracy, particularly for the ground ($X\ ^1\Sigma_g^+$) and first excited ($b\ ^3\Sigma_u^+$) states. In Figures 1 and 2 the PECs calculated in the spheroidal model are presented for the singlet and triplet states, and compared with the accurate calculations of references [50,55,60,61]. We find excellent agreement for all states up to $R = 5.0$, which is sufficient to model collisions with vibrationally excited $H_2(X\ ^1\Sigma_g^+, v_i)$ with $v_i = 0$–12, and good agreement (within 3%) up to $R = 8.0$, which is required to model scattering on the remaining $v_i = 13$–14 levels.

Table 2 presents the optical oscillator strengths (OOS) for a number of optically allowed transitions calculated at $R = 1.4$. We find very good agreement between the length and velocity forms for the spheroidal approach and similarly good agreement with previous calculations [50,62]. The spherical approach shows reasonable agreement with the previous calculations, in particular for the length form, though for the $B\ ^1\Sigma_u^+$ state the length form is 9% too low. Figure 3 presents the dependence of the OOS on the

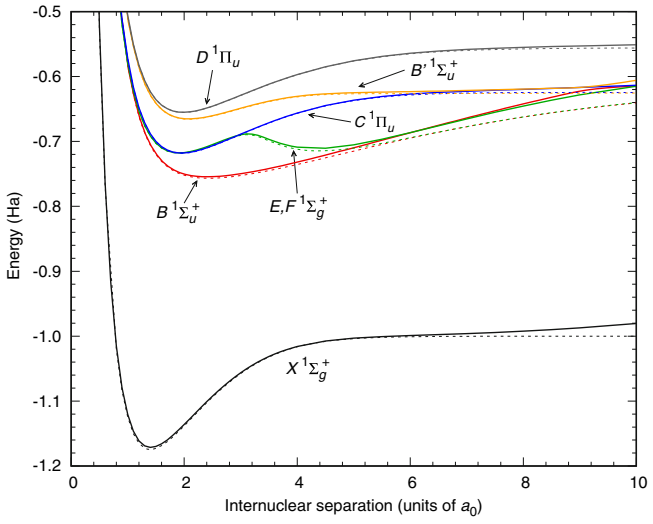

Fig. 1. The present potential-energy curves for several singlet states of H_2 (solid lines), compared with accurate calculations (dashed lines) obtained for the $X\ ^1\Sigma_g^+$ state from reference [60], the $B\ ^1\Sigma_u^+$ and $B'\ ^1\Sigma_u^+$ states from reference [55], the $C\ ^1\Pi_u$ and $D\ ^1\Pi_u$ states from reference [50], and the $E, F\ ^1\Sigma_g^+$ state from reference [61].

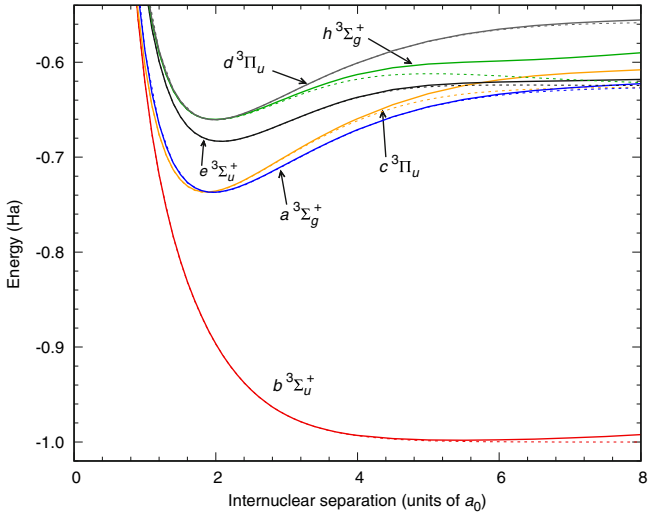

Fig. 2. The present potential-energy curves for several triplet states of H_2 (solid lines), compared with accurate calculations (dashed lines) obtained from reference [59].

internuclear distance up to $R = 8.0$. Similar to the energies obtained in the spheroidal approach, we find very good agreement with the accurate calculations [50,62] for $R \leq 5.0$ with only small errors at larger internuclear distances.

4 Results

In Figures 4 and 5 we present cross sections summed over all final vibrational levels in the $B\ ^1\Sigma_u^+$, $C\ ^1\Pi_u$, $B'\ ^1\Sigma_u^+$, $D\ ^1\Pi_u$ and $E, F\ ^1\Sigma_g^+$ singlet states and the $b\ ^3\Sigma_u^+$, $c\ ^3\Pi_u$, $a\ ^3\Sigma_g^+$, $e\ ^3\Sigma_u^+$, $h\ ^3\Sigma_g^+$, and $d\ ^3\Pi_u$ triplet states, for

Table 2. Optical oscillator strengths (OOS) for transitions from the $X\ ^1\Sigma_g^+$ state to the $B\ ^1\Sigma_u^+$, $C\ ^1\Pi_u$, $B'\ ^1\Sigma_u^+$, and $D\ ^1\Pi_u$ states of H_2 at the internuclear separation $R = 1.4\ a_0$. Results from the present spherical- and spheroidal-coordinate structure calculations performed in the length (L) and velocity (V) forms are compared with the accurate calculations of references [50,62].

State	Spherical		Spheroidal		Refs.
	L	V	L	V	[50,62]
$B\ ^1\Sigma_u^+$	0.277	0.243	0.298	0.293	0.301
$C\ ^1\Pi_u$	0.337	0.312	0.357	0.352	0.358
$B'\ ^1\Sigma_u^+$	0.058	0.050	0.057	0.058	0.057
$D\ ^1\Pi_u$	0.083	0.077	0.086	0.085	0.085

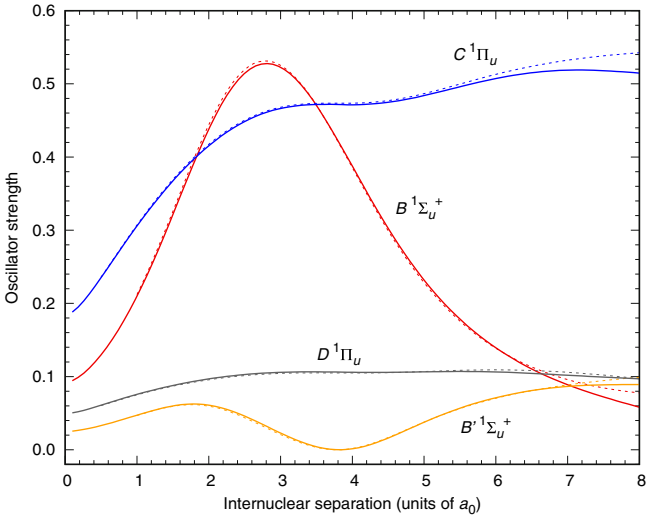

Fig. 3. Optical oscillator strengths (OOS) between the $X\ ^1\Sigma_g^+$ state and several singlet states of H_2. Results of the present spheroidal-coordinate structure calculation (solid lines) are compared with accurate calculations (dashed lines) obtained from references [50,62].

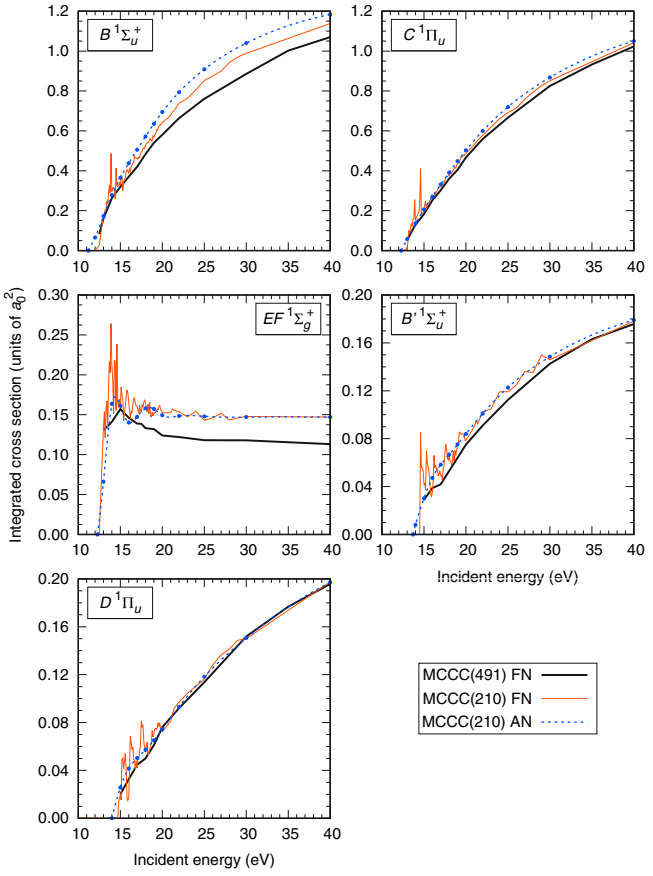

Fig. 4. Electron-impact excitation cross sections summed over all final vibrational levels in the $B\ ^1\Sigma_u^+$, $C\ ^1\Pi_u$, $B'\ ^1\Sigma_u^+$, $D\ ^1\Pi_u$, and $E, F\ ^1\Sigma_g^+$ states for scattering on the $X\ ^1\Sigma_g^+(v_i = 0)$ ground state of H_2. Fixed-nuclei (FN) results of the spherical MCCC(491) and spheroidal MCCC(210) models are presented, as well as adiabatic-nuclei (AN) calculations performed with the spheroidal MCCC(210) model.

electrons scattering on the $X\ ^1\Sigma_g^+(v_i = 0)$ ground state of H_2. In this investigation we concentrate on the low to intermediate incident electron energy range, from 6 to 40 eV. For all excitations we present results from three calculations: the FN spherical MCCC(491) model, the FN spheroidal MCCC(210) model, and the AN spheroidal MCCC(210) model (with scaling, as described in Sect. 3). For clarity of presentation, we have not included experimental data points in Figures 4 and 5, however detailed comparisons of the MCCC(491) cross sections with experiment can be found in references [16,33].

The FN MCCC(210) calculations were performed on a fine energy mesh at $R = 1.448$. The calculations show numerous resonance structures for practically all transitions that diminish with increasing incident energy. These could be a combination of true resonances, pseudoresonances related to the relatively small size of the close-coupling expansion in the MCCC(210) model, and numerical instabilities. The spherical MCCC(491) model, performed also at $R = 1.448$, has a much larger close-coupling expansion and therefore is significantly less affected by pseudo resonances. It generally produces smoother cross sections, though the choice of incident energies at which the calculations were performed could be fortuitous.

The calculations performed in the AN formulation of the MCCC(210) model were conducted at a set of incident energies that was sufficient to map out excitation cross sections. It is prohibitively computationally expensive to conduct the AN MCCC(210) calculations on a fine energy mesh. However, we have performed such calculations with smaller models. In reference [49] we used a 12-state model in the spherical formulation to perform AN calculations with the aim of producing AN cross sections for excitation of the $b\ ^3\Sigma_u^+$ state from the $X\ ^1\Sigma_g^+(v_i = 0)$ ground state of H_2. These calculations are in very good agreement with the AN MCCC(210) results for the $b\ ^3\Sigma_u^+$ state. We showed that the FN MCC(12) cross section for the $b\ ^3\Sigma_u^+$ state exhibits a number of sharp resonance structures that change their energy position with changing R. However, the effective averaging procedure over R in equation (21)

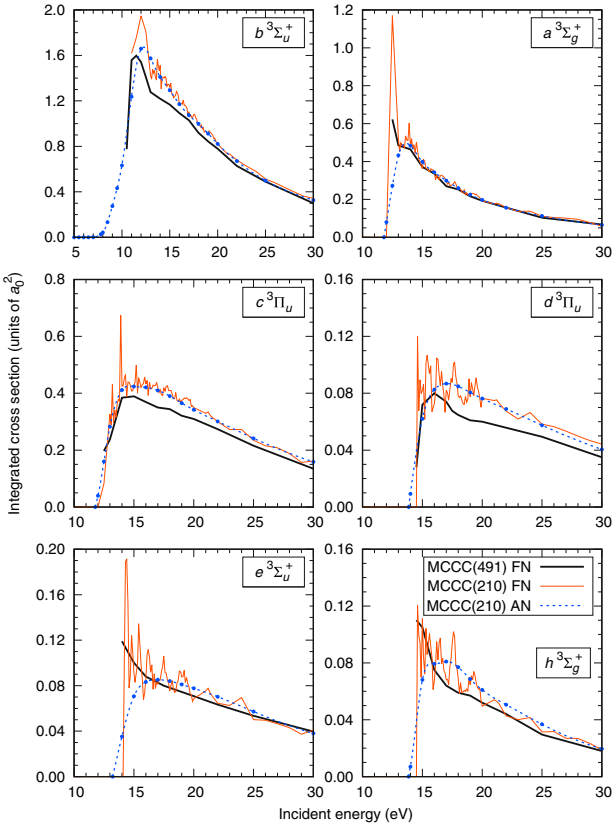

Fig. 5. Electron-impact excitation cross sections summed over all final vibrational levels in the $b\ ^3\Sigma_u^+$, $c\ ^3\Pi_u$, $a\ ^3\Sigma_g^+$, $e\ ^3\Sigma_u^+$, $h\ ^3\Sigma_g^+$, and $d\ ^3\Pi_u$ states for scattering on the $X\ ^1\Sigma_g^+(v_i = 0)$ ground state of H_2. Fixed-nuclei (FN) results of the spherical MCCC(491) and spheroidal MCCC(210) models are presented, as well as adiabatic-nuclei (AN) calculations performed with the spheroidal MCCC(210) model.

leads to a smooth AN cross section. We have performed AN calculations using the spheroidal MCC(27) model and found similar behaviour for other electronic transitions – the sharper resonance structures tend to disappear in the AN approach while broader structures are diminished in magnitude. The AN MCCC(210) cross sections show similar behaviour as can be seen from Figures 4 and 5. We therefore believe that smooth interpolation between the energies of the AN MCCC(210) results should lead to sufficiently accurate cross-section estimates. We note that similar smoothing behaviour in the AN method was found in reference [63] in their studies of dissociative excitation of HeH^+ by electron impact, where the FN cross sections showed a number of strong resonance peaks.

The AN MCCC(210) calculations together with our previous AN MCC(12) results for the $b\ ^3\Sigma_u^+$ state provide a set of cross sections for incident electron energies close to excitation thresholds for a large number of excited states of H_2 (a complete set of vibrationally resolved cross sections is in preparation [64]). At low energies the AN cross sections differ substantially from the corresponding FN cross sections for the triplet-state excitations and dipole-forbidden transitions, which generally have a sharp rise at the threshold. For excitation of the dipole-allowed transitions, which rise smoothly from threshold, the difference between the FN and AN cross sections is not as significant.

For a number of transitions there are systematic differences between the spheroidal MCCC(210) cross sections and the corresponding cross sections of the spherical MCCC(491) model. This is primarily due to the more accurate target structure in the spheroidal formulation. For example, the $B\ ^1\Sigma_u^+$ MCCC(210) cross section is larger than the MCCC(491) cross section, due to the OOS for this transition being less accurate in the MCCC(491) model. As discussed earlier, the OOS from the spherical structure model are too low by about 9%, and this translates to a comparable error in the excitation cross sections. Similar systematic differences were found for the $E, F\ ^1\Sigma_g^+$ state, where the spheroidal MCCC(210) cross section is larger by nearly 30% than the MCCC(491) cross section for incident energies above 20 eV. Smaller, but still substantial differences have been found for a number of triplet states ($c\ ^3\Pi_u$, $d\ ^3\Pi_u$, and $h\ ^3\Sigma_g^+$). Importantly, we find good agreement between the spherical and spheroidal MCCC results for the $C\ ^1\Pi_u$ excitation, where there still exists a large discrepancy between theory and the recommended cross sections (derived from experiment) at intermediate and high energies [16].

In Figures 6 and 7 we present differential cross sections (DCS) for excitation of the singlet $B\ ^1\Sigma_u^+$, $C\ ^1\Pi_u$, $E, F\ ^1\Sigma_g^+$, and triplet $b\ ^3\Sigma_u^+$, $a\ ^3\Sigma_g^+$, and $c\ ^3\Pi_u$ states from the $X\ ^1\Sigma_g^+(v_i = 0)$ ground state of H_2. Results of the spherical MCCC(491) and spheroidal MCCC(210) FN models are compared with available measurements at incident energies between 15 and 20 eV for the triplet states, and 20 and 30 eV for the singlet states. The overall shapes of the DCS are similar in the two MCCC formulations, with differences in magnitude for some states as consistent with the ICS results presented in Figures 4 and 5.

5 Conclusions

We have presented a comparison of the cross sections calculated in the spherical- and spheroidal-coordinate formulations of the MCCC method. The more accurate target structure in the spheroidal calculations makes the calculated collision cross sections more accurate. Generally good agreement is found between the spherical FN MCCC(491) and spheroidal FN MCCC(210) cross sections. However, for a number of transitions the differences were substantial (up to 30%).

The spheroidal FN MCCC(210) calculations have been performed on a fine energy mesh for $R = 1.448$. The numerous resonance structures found in these FN calculations tend to disappear when the AN approach is applied to calculations of the collision cross sections. The AN MCCC(210) calculations have allowed us to produce a comprehensive set of cross sections with vibrational levels resolved in both the initial and final electronic states. Here we presented a set of AN cross sections for scattering on the $X\ ^1\Sigma_g^+(v_i = 0)$ ground state of H_2. These cross sections represent a reliable estimate at near-threshold energies, where the FN approach fails. At higher incident

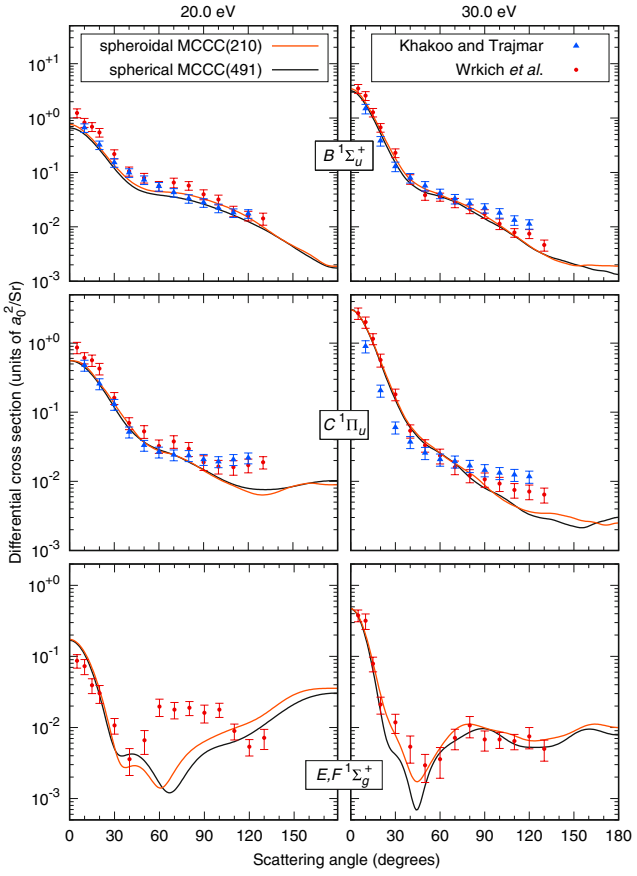

Fig. 6. Electron-impact differential cross sections for excitation of the $B\ ^1\Sigma_u^+$, $C\ ^1\Pi_u$, and $E, F\ ^1\Sigma_g^+$ states by 20- and 30 eV electrons scattering on the $X\ ^1\Sigma_g^+(v_i = 0)$ ground state of H_2. Fixed-nuclei results of the spheroidal MCCC(210) and spherical MCCC(491) models are compared with the measurements of Khakoo and Trajmar [65] and Wrkich et al. [66].

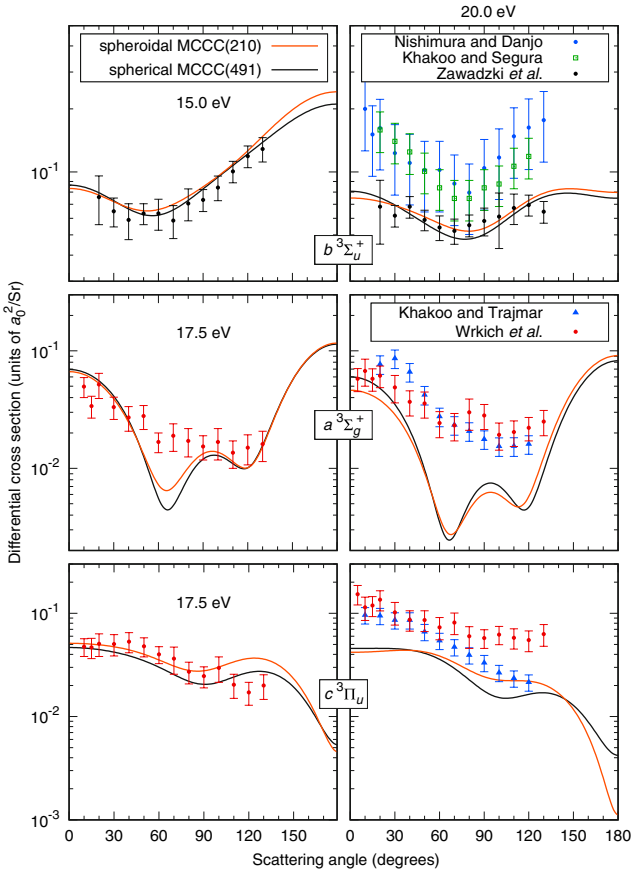

Fig. 7. Electron-impact differential cross sections for excitation of the $b\ ^3\Sigma_u^+$, $c\ ^3\Pi_u$, and $a\ ^3\Sigma_g^+$ states by 15-, 17.5-, and 20 eV electrons scattering on the $X\ ^1\Sigma_g^+(v_i = 0)$ ground state of H_2. Fixed-nuclei results of the spheroidal MCCC(210) and spherical MCCC(491) models are compared with the measurements of Nishimura and Danjo [67], Khakoo and Segura [68], Zawadzki et al. [33], Khakoo and Trajmar [65], and Wrkich et al. [66].

energies, the FN cross sections are an excellent approximation to the AN cross sections summed over final vibrational levels.

We hope the present results will be of interest to the plasma-modelling community. Future work in the MCCC project will include more accurate calculations of low-energy elastic and excitation cross sections using a vibrational close-coupling method, and the extension to more complex molecular targets.

This work was supported by the United States Air Force Office of Scientific Research, Los Alamos National Laboratory (LANL), Curtin University, and resources provided by the Pawsey Supercomputing Centre, with funding from the Australian Government and Government of Western Australia. L.H.S. acknowledges the contribution of an Australian Government Research Training Program Scholarship, and the support of the Forrest Research Foundation. M.C.Z. would like to specifically acknowledge LANL's ASC PEM Atomic Physics Project for its support. LANL is operated by Triad National Security, LLC, for the National Nuclear Security Administration of the U.S. Department of Energy under contract No. 89233218NCA000001.

Author contribution statement

L.H.S. and D.V.F. wrote the manuscript. All authors discussed the results and commented on the manuscript. J.S.S., D.V.F., M.C.Z., and I.B. developed the underlying theoretical techniques and code. L.H.S. performed the AN calculations.

References

1. C.M. Samuell, C.S. Corr, Plasma Sources Sci. Technol. **25**, 015014 (2016)
2. K. Sawada, M. Goto, Atoms **4**, 29 (2016)
3. D. Shemansky, X. Liu, H. Melin, Planet. Space Sci. **57**, 1659 (2009)
4. H. Melin, D.E. Shemansky, X. Liu, Planet. Space Sci. **57**, 1743 (2009)
5. H. Abgrall, E. Roueff, X. Liu, D.E. Shemansky, ApJ **481**, 557 (1997)
6. T. Stephens, A. Dalgarno, J. Quant. Spectrosc. Radiat. Transfer **12**, 569 (1972)

7. Y. Ju, W. Sun, Prog. Energy Combust. Sci. **48**, 21 (2015)
8. W.T. Miles, R. Thompson, A.E.S. Green, J. Appl. Phys. **43**, 678 (1972)
9. H. Tawara, Y. Itikawa, H. Nishimura, M. Yoshino, J. Phys. Chem. Ref. Data **19**, 617 (1990)
10. A. Zecca, G.P. Karwasz, R.S. Brusa, Riv. Nuovo Cimento **19**, 1 (1996)
11. M.J. Brunger, S.J. Buckman, Phys. Rep. **357**, 215 (2002)
12. B.G. Lindsay, M.A. Mangan, in *Photon and Electron Interactions with Atoms, Molecules and Ions, Landolt-Börnstein, New Series, Goup I, Pt. C*, edited by Y. Itikawa (Springer, New York, 2003), Vol. 17
13. R. Janev, D. Reiter, U. Samm, Collision processes in low-temperature hydrogen plasmas, Forschungszentrum Jülich, Zentralbibliothek, 2003
14. J.S. Yoon, M.Y. Song, J.M. Han, S.H. Hwang, W.S. Chang, B. Lee, Y. Itikawa, J. Phys. Chem. Ref. Data **37**, 913 (2008)
15. D.V. Fursa, M.C. Zammit, R.L. Threlfall, J.S. Savage, I. Bray, Phys. Rev. A **96**, 022709 (2017)
16. M.C. Zammit, J.S. Savage, D.V. Fursa, I. Bray, Phys. Rev. A **95**, 022708 (2017)
17. M.C. Zammit, J.S. Savage, D.V. Fursa, I. Bray, Phys. Rev. Lett. **116**, 233201 (2016)
18. T.N. Rescigno, C.W. McCurdy, V. McKoy, C.F. Bender, Phys. Rev. A **13**, 216 (1976)
19. A.W. Fliflet, V. McKoy, Phys. Rev. A **21**, 1863 (1980)
20. L. Mu-Tao, R.R. Lucchese, V. McKoy, Phys. Rev. A **26**, 3240 (1982)
21. T.N. Rescigno, B.I. Schneider, J. Phys. B: At., Mol. Opt. Phys. **21**, L691 (1988)
22. S.D. Parker, C.W. McCurdy, T.N. Rescigno, B.H. Lengsfield, Phys. Rev. A **43**, 3514 (1991)
23. M.A.P. Lima, T.L. Gibson, W.M. Huo, V. McKoy, J. Phys. B: At., Mol. Opt. Phys. **18**, L865 (1985)
24. T.L. Gibson, M.A.P. Lima, V. McKoy, W.M. Huo, Phys. Rev. A **35**, 2473 (1987)
25. M.A.P. Lima, T.L. Gibson, V. McKoy, W.M. Huo, Phys. Rev. A **38**, 4527 (1988)
26. B.I. Schneider, L.A. Collins, J. Phys. B: At., Mol. Opt. Phys. **18**, L857 (1985)
27. A.M. Machado, M.M. Fujimoto, A.M.A. Taveira, L.M. Brescansin, M.T. Lee, Phys. Rev. A **63**, 032707 (2001)
28. S.E. Branchett, J. Tennyson, L.A. Morgan, J. Phys. B: At., Mol. Opt. Phys. **23**, 4625 (1990)
29. S.E. Branchett, J. Tennyson, L.A. Morgan, J. Phys. B: At., Mol. Opt. Phys. **24**, 3479 (1991)
30. R.F. da Costa, F.J. da Paixão, M.A.P. Lima, J. Phys. B: At., Mol. Opt. Phys. **38**, 4363 (2005)
31. L.R. Hargreaves, S. Bhari, B. Adjari, X. Liu, R. Laher, M. Zammit, J.S. Savage, D.V. Fursa, I. Bray, M.A. Khakoo, J. Phys. B: At., Mol. Opt. Phys. **50**, 225203 (2017)
32. M. Zawadzki, M.A. Khakoo, Phys. Rev. A **99**, 042703 (2019)
33. M. Zawadzki, R. Wright, G. Dolmat, M.F. Martin, B. Diaz, L. Hargreaves, D. Coleman, D.V. Fursa, M.C. Zammit, L.H. Scarlett, J.K. Tapley, J.S. Savage, I. Bray, M.A. Khakoo, Phys. Rev. A **98**, 062704 (2018)
34. M. Zawadzki, R. Wright, G. Dolmat, M.F. Martin, L. Hargreaves, D.V. Fursa, M.C. Zammit, L.H. Scarlett, J.K. Tapley, J.S. Savage, I. Bray, M.A. Khakoo, Phys. Rev. A **97**, 050702(R) (2018)
35. N.F. Lane, Rev. Mod. Phys. **52**, 29 (1980)
36. R. Celiberto, M. Capitelli, A. Laricchiuta, Phys. Scr. **2002**, 32 (2002)
37. A. Laricchiuta, R. Celiberto, F. Esposito, M. Capitelli, Plasma Sources Sci. Technol. **15**, S62 (2006)
38. G. Colonna, L.D. Pietanza, G. D'Ammando, R. Celiberto, M. Capitelli, A. Laricchiuta, Eur. Phys. J. D **71**, 279 (2017)
39. L.H. Scarlett, J.S. Savage, D.V. Fursa, M.C. Zammit, I. Bray, Atoms **7** (2019)
40. J.K. Tapley, L.H. Scarlett, J.S. Savage, D.V. Fursa, M.C. Zammit, I. Bray, Phys. Rev. A **98**, 032701 (2018)
41. J.K. Tapley, L.H. Scarlett, J.S. Savage, M.C. Zammit, D.V. Fursa, I. Bray, J. Phys. B: At., Mol. Opt. Phys. **51**, 144007 (2018)
42. L.H. Scarlett, J.K. Tapley, D.V. Fursa, M.C. Zammit, J.S. Savage, I. Bray, Eur. Phys. J. D **72**, 34 (2018)
43. L.H. Scarlett, J.K. Tapley, J.S. Savage, D.V. Fursa, M.C. Zammit, I. Bray, Plasma Sources Sci. Technol. **28**, 025004 (2019)
44. M.C. Zammit, D.V. Fursa, J.S. Savage, I. Bray, J. Phys. B: At., Mol. Opt. Phys. **50**, 123001 (2017)
45. M.C. Zammit, D.V. Fursa, I. Bray, Phys. Rev. A **90**, 022711 (2014)
46. M.C. Zammit, J.S. Savage, J. Colgan, D.V. Fursa, D.P. Kilcrease, I. Bray, C.J. Fontes, P. Hakel, E. Timmermans, Astrophys. J. **64**, 851 (2017)
47. I. Bray, A.T. Stelbovics, Phys. Rev. A **46**, 6995 (1992)
48. J.Y. Zhang, J. Mitroy, Phys. Rev. A **83**, 022711 (2011)
49. L.H. Scarlett, J.K. Tapley, D.V. Fursa, M.C. Zammit, J.S. Savage, I. Bray, Phys. Rev. A **96**, 062708 (2017)
50. L. Wolniewicz, G. Staszewska, J. Mol. Spectrosc. **220**, 45 (2003)
51. W. Kolos, K. Szalewicz, H.J. Monkhorst, J. Chem. Phys. **84**, 3278 (1986)
52. W. Kolos, L. Wolniewicz, J. Chem. Phys. **43**, 2429 (1965)
53. W. Kolos, L. Wolniewicz, J. Chem. Phys. **48**, 3672 (1968)
54. W. Kolos, J. Rychlewski, J. Mol. Spectrosc. **66**, 428 (1977)
55. G. Staszewska, L. Wolniewicz, J. Mol. Spectrosc. **212**, 208 (2002)
56. J.W. Liu, S. Hagstrom, Phys. Rev. A **48**, 166 (1993)
57. W. Kolos, J. Rychlewski, J. Mol. Spectrosc. **143**, 237 (1990)
58. T.E. Sharp, At., Data Nucl. Data Tables **2**, 119 (1971)
59. G. Staszewska, L. Wolniewicz, J. Mol. Spectrosc. **198**, 416 (1999)
60. L. Wolniewicz, J. Chem. Phys. **99**, 1851 (1993)
61. T. Orlikowski, G. Staszewska, L. Wolniewicz, Mol. Phys. **96**, 1445 (1999)
62. L. Wolniewicz, G. Staszewska, J. Mol. Spectrosc. **217**, 181 (2003)
63. A.E. Orel, T.N. Rescigno, B.H. Lengsfield, Phys. Rev. A **44**, 4328 (1991)
64. L.H. Scarlett, D.V. Fursa, M.C. Zammit, I. Bray, Yu. Ralchenko, K. Davie, At., Data Nucl. Data Tables (2020, submitted)
65. M.A. Khakoo, S. Trajmar, Phys. Rev. A **34**, 138 (1986)
66. J. Wrkich, D. Mathews, I. Kanik, S. Trajmar, M.A. Khakoo, J. Phys. B: At., Mol. Opt. Phys. **35**, 4695 (2002)
67. H. Nishimura, A. Danjo, J. Phys. Soc. Jpn. **55**, 3031 (1986)
68. E. Krishnakumar, S.K. Srivastava, J. Phys. B: At., Mol. Opt. Phys. **27**, L251 (1994)